Burnett Description for plane Poiseuille flow

F.J. Uribe
Physics Department, Universidad Autónoma Metropolitana Iztapalapa, P.O. Box 55-534, 09340 México D.F.
and
Alejandro L. Garcia*
Center for Computational Sciences and Engineering, Lawrence Berkeley National Laboratory, Berkeley, Calf. 94720, USA.
PACS numbers:05.20.Dd, 05.60.+w, 02.70.Ns, 47.45.-n, 47.45.Gx.

Two recent works have shown that at small Knudsen number (K) the pressure and temperature profiles in plane Poiseuille flow exhibit a different qualitative behavior from the profiles obtained by the Navier-Stokes equations. Tij and Santos [J. Stat. Phys. **76**(1994)1399.] used the Bhatnagar-Gross-Kook (BGK) model to show that the temperature profile is bimodal and the pressure profile is non-constant. Malek-Mansour, Baras and Garcia [Physica **A240**(1997)255.] qualitatively confirmed these predictions in computer experiments using the Direct Simulation Monte Carlo method (DSMC). In this paper we compare the DSMC measurements of hydrodynamic variables and non-equilibrium fluxes with numerical solutions of the Burnett equations. Given that they are in better agreement with Molecular Dynamics (MD) simulations of strong shock waves than Navier-Stokes [F.J. Uribe, R.M. Velasco and L.S. García-Colín, Phys. Rev. Lett. **81**(1998)2044.], and that they are second order in Knudsen number suggests that the Burnett equations may provide a better description for large K. We find that for plane Poiseuille flow the Burnett equations do not predict the bimodal temperature profile but do recover many of the other anomalous features (e.g., non-constant pressure and non-zero parallel heat flux).

I. INTRODUCTION

The Navier-Stokes equations provide a sound and robust theoretical method to study flows at the macroscopic level which have innumerable applications. The complexity of the equations is due to the fact that they are nonlinear except for simple cases where, due mainly to the symmetries involved, they reduce to linear equations that can be solved in closed form. The Navier-Stokes equations can be derived from strictly macroscopic arguments or from a Kinetic model, such as the Boltzmann equation for dilute gases, however, their derivation assumes both the local equilibrium hypotheses and the small gradients approximation, which allows one to formulate the constitutive equations needed to close the conservation equations. In situations where large gradients exist, as in a shock wave or in a boundary layer, these equations are expected to fail, as has been pointed out in the past. Furthermore, being a macroscopic theory their validity is also restricted to situations in which the Knudsen number (K) is small and a crucial point is to know, for a given problem, the range of Knudsen numbers where they remain valid. Another important parameter is the Reynolds number (R_e) which in some cases determines when the solutions cease to be laminar and the flow becomes turbulent.

The Navier-Stokes equations can, in principle, be solved as an initial value problem. Usually stick boundary conditions are used but when the Knudsen number is not small ($K > 10^{-2}$) the slip at the boundaries must be taken into account [1]. There exist simple examples in which the solutions to the stationary Navier-Stokes equations are infinite (countable) even for fixed Reynolds number [2] so even when only one solution exists, as in plane Poiseuille flow with stick boundary conditions, one needs to perform a stability analysis of the solutions [3].

Recently Tij and Santos [4] showed that a perturbative solution to the Bhatnagar-Gross-Kook (BGK) model predicted qualitatively different temperature and pressure profiles from those predicted by the Navier-Stokes equations. Mansour *et al.* [5] confirmed this result using the Direct Simulation Monte Carlo method (DSMC) to model plane Poiseuille flow of a dilute hard sphere gas for $R_e \approx 10$ and $K = 1/10$. Mansour *et al.* also solved the Navier-Stokes equations numerically and showed that slip corrections could not explain the discrepancy. The results obtained by Tij and Santos are in better quantitative agreement with the DSMC data if the Chapman-Cowling expressions for the transport coefficients are used instead of the those derived from the BGK model, which give an incorrect Euken factor. While the Euken factor is in contradiction with the results from both the Chapman-Enskog method and experiment, it should be pointed out that the BGK model is able to repro-

*Permanent address: Physics Dept., San Jose State University, San Jose, Calf. 95192, USA.

duce qualitative features in situations far from equilibrium where the Chapman-Enskog method is not applicable and so the model is useful as a guide in such situations.

To the authors' knowledge Poiseuille flow is the first scenario in which the Navier-Stokes equations have been shown to be susceptible to significant improvement for a flow with relatively small gradients. Since Uribe *et al.* [6] showed that the Burnett equations can provide an accurate description for strong shock waves, it is then a natural step to compare the Burnett equations with DSMC simulations of Poiseuille flow and that is what we do here. The next four sections present the theoretical development of the conservation equations, the Navier-Stokes equations, the Burnett equations and the Burnett fluxes. The DSMC algorithm is outlined briefly in section VI; simulation results are presented and discussed in sections VII and VIII. Section IX contains final remarks and a discussion of future work.

II. THE CONSERVATION EQUATIONS

We consider the flow between two infinite and stationary plane parallel walls located a $y = \pm L/2$. The hydrodynamic velocity, $\mathbf{c}_0$, is assumed to have only an x-component so that $\mathbf{c}_0 \equiv \mathbf{u} = u(\mathbf{r}, t)\mathbf{i}$ in the laminar, stationary case (unless stated otherwise, we adopt the notation used by Chapman and Cowling [7]). Following Landau and Lifshitz [8] we assume that all the relevant quantities can only depend on the y coordinate, in particular $\mathbf{c}_0 = u(y)\mathbf{i}$. Noting that for any function, $f(y)$, $(\mathbf{c}_0 \cdot \nabla) f(y) = 0$ it follows that the conservation equations reduce to:

$$0 = \nabla \cdot \Big(\rho(y) u(y)\mathbf{i}\Big), \tag{1}$$

$$0 = -\frac{1}{\rho(y)}\frac{d\,\mathbf{P}_{yx}}{d\,y} + a \tag{2}$$

$$0 = -\frac{1}{\rho(y)}\frac{d\,\mathbf{P}_{yy}}{d\,y}, \tag{3}$$

$$0 = -\frac{1}{\rho(y)}\frac{d\,\mathbf{P}_{yz}}{d\,y}, \tag{4}$$

$$0 = \mathbf{P}_{yx}\frac{d\,u(y)}{d\,y} + \frac{d\,q_y(y)}{d\,y}, \tag{5}$$

where $\rho(y)$ is the mass density, $\mathbf{P}(y)$ the pressure tensor, $\mathbf{q}(y)$ the heat flux, and a the acceleration from a constant, external body force (e.g., gravity) acting in the x direction. Eq. (1) is the mass conservation equation which is automatically satisfied, eqs. (2), (3) and (4) are the components of Newton's second law (momentum conservation) and eq. (5) is the energy conservation equation. Notice that we can conclude that the components $\mathbf{P}_{yy}$ and $\mathbf{P}_{yz}$ of the pressure tensor are constant, a result that does not depend on the constitutive relations.

For the discussion that follows it is important to keep in mind that the results of this section depend on the three conditions: (1) $\mathbf{u}_y = 0$; (2) $\mathbf{u}_z = 0$ and (3) All the physical quantities depend only on y. The last condition will be referred to as Landau's symmetry argument.

In a dilute gas the pressure $p(y)$ and temperature $T(y)$ are related by the ideal gas equation of state $p = \rho\, k\, T/m$ where m is the particle mass and k is Boltzmann's constant. To have a closed system in the variables $u(y)$, $p(y)$ and $T(y)$ one needs to introduce constitutive relations. Since the contributions up to second order in the Knudsen number for the pressure tensor and heat flux include the Navier-Stokes terms (first order in the Knudsen number) these terms are developed in the next section.

III. THE NAVIER-STOKES REGIME

The Navier-Stokes expressions for the pressure tensor ($\mathbf{P}^{NS}$) and the heat flow ($\mathbf{q}^{NS}$) are given by:

$$\mathbf{P}^{NS} = p\,\mathbf{I} - 2\,\mu\,\overset{\circ}{\overline{\overline{\nabla\,\mathbf{c}_0}}} \quad , \tag{6}$$

$$\mathbf{q}^{NS} = -\lambda\,\nabla T, \tag{7}$$

where μ is the shear viscosity, λ the thermal conductivity and I is the unit tensor. The double overbar denotes the symmetric tensor and the circle means the corresponding traceless tensor. For stationary, plane Poiseuille flow these constitutive relations simplify to:

$$\begin{aligned} \mathbf{P}^{NS}_{yx} &= -\mu\,\frac{d\,u(y)}{d\,y}, \\ \mathbf{P}^{NS}_{yy} &= p(y), \\ \mathbf{P}^{NS}_{yz} &= 0, \\ \mathbf{q}^{NS}_{y} &= -\lambda\frac{d\,T(y)}{d\,y}, \end{aligned} \tag{8}$$

For a dilute gas of rigid spheres the transport coefficients are [7],

$$\mu = \frac{5\,c_{\mu}}{16\,\sigma^2}\left(\frac{m\,k\,T(y)}{\pi}\right)^{1/2}, \quad \lambda = \frac{75\,c_{\lambda}}{64\,\sigma^2}\left(\frac{k^2\,T(y)}{\pi\,m}\right)^{1/2}. \tag{9}$$

where σ is the particle diameter. While often the transport coefficients are approximated by the first Sonine expansion ($c_{\mu} = c_{\lambda} = 1$), for rigid spheres more precise values ($c_{\mu} = 1.016034$, $c_{\lambda} = 1.02513$) are known [7].

Substitution of eqs. (8) and (9) into eqs. (1)-(5) leads us to:

$$
\begin{aligned}
10\, c_\mu\, k^2\, T(y)^2 \frac{d^2 u}{d y^2} &= -5\, c_\mu\, k^2\, T(y) \frac{d T}{d y} \frac{d u}{d y} \\
&\quad - 32\, p\, \sigma^2\, a \left(\pi\, m\, k\, T(y)\right)^{1/2}, \\
30\, c_\lambda\, k^3\, T(y) \frac{d^2 T}{d y^2} &= -8\; m\, c_\mu\, k^2\, T(y)^2 \left(\frac{d u}{d y}\right)^2 \\
&\quad - 15\, c_\lambda\, k^3 \left(\frac{d T}{d y}\right)^2, \qquad (10)
\end{aligned}
$$

Note that in the Navier-Stokes regime the pressure is constant so we have two second order nonlinear equations for u and T. The boundary conditions for these equations are discussed in the next section.

IV. THE BURNETT REGIME

The second order Knudsen number corrections for the stress tensor ($\mathbf{P}^{(2)}$) and the heat flux ($\mathbf{q}^{(2)}$) are given by [7]:

$$
\begin{aligned}
\mathbf{P}^{(2)} &= \omega_1 \frac{\mu^2}{p}\, \Delta\, \overset{\circ}{\mathbf{e}} + \omega_2 \frac{\mu^2}{p} \left\{ \frac{D_0}{D\,t}\, \overset{\circ}{\mathbf{e}} - 2 \overset{\circ}{\overline{\overline{\nabla \mathbf{c}_0 \cdot \overset{\circ}{\mathbf{e}}}}} \right\} \\
&\quad + \omega_3 \frac{\mu^2}{\rho T} \overset{\circ}{\overline{\overline{\nabla\nabla T}}} + \omega_4 \frac{\mu^2}{\rho p T} \overset{\circ}{\overline{\overline{\nabla p\, \nabla T}}} \\
&\quad + \omega_5 \frac{\mu^2}{\rho T^2} \overset{\circ}{\overline{\overline{\nabla T\, \nabla T}}} + \omega_6 \frac{\mu^2}{\rho T} \overset{\circ}{\overline{\overline{\overset{\circ}{\mathbf{e}} \cdot \overset{\circ}{\mathbf{e}}}}}, \\
\mathbf{q}^{(2)} &= \theta_1 \frac{\mu^2}{\rho T}\, \Delta\, \nabla T + \theta_2 \frac{\mu^2}{\rho T} \left\{ \frac{D_0}{D\,t} \nabla T - \nabla \mathbf{c}_0 \cdot \nabla T \right\} \\
&\quad + \theta_3 \frac{\mu^2}{\rho T} \nabla p \cdot \overset{\circ}{\mathbf{e}} + \theta_4 \frac{\mu^2}{\rho} \nabla \cdot \overset{\circ}{\mathbf{e}} + \theta_5 \frac{3\mu^2}{\rho T} \nabla T \cdot \overset{\circ}{\mathbf{e}},
\end{aligned}
\qquad (11)
$$

where the numerical values for the ω's and θ's are given below and [7]

$$
\begin{aligned}
&\mathbf{e} = \overline{\overline{\nabla \mathbf{c}_0}}, \quad \Delta = \nabla \cdot \mathbf{c}_0, \\
&\frac{D_0}{D\,t}\left(\nabla T\right) = -\frac{2}{3} \nabla \left(T\, \nabla \cdot \mathbf{c}_0\right) - \left(\nabla \mathbf{c}_0 \cdot \nabla T\right) \\
&\frac{D_0}{D\,t}\left(\overset{\circ}{\mathbf{e}}\right) = \overset{\circ}{\overline{\overline{\nabla\left(\mathbf{a} - \frac{1}{\rho} \nabla p\right)}}} - \overset{\circ}{\overline{\overline{\nabla \mathbf{c}_0 \cdot \nabla \mathbf{c}_0}}}\,.
\end{aligned}
\qquad (12)
$$

For plane Poiseuille flow we are lead to:

$$
\begin{aligned}
\mathbf{P}^{(2)}_{yx} &= 0, \quad \mathbf{P}^{(2)}_{yz} = 0, \\
\mathbf{P}^{(2)}_{yy} &= \frac{2}{3} \frac{\omega_2\, \mu^2}{p(y)\, \rho(y)} \frac{d\, p}{d\, y} \frac{d\, \rho}{d\, y} - \frac{2}{3} \frac{\omega_2\, \mu^2}{p(y)\, \rho(y)} \frac{d^2\, p}{d\, y^2} - \frac{3}{4} \frac{\omega_2\, \mu^2}{p(y)} \\
&\quad \times \left(\frac{d\, u}{d\, y}\right)^2 + \frac{2}{3} \frac{\omega_3\, \mu^2}{T(y)\, \rho(y)} \frac{d^2\, T}{d\, y^2} + \frac{2}{3} \frac{\omega_4\, \mu^2}{p(y)\, T(y)\, \rho(y)} \\
&\quad \times \frac{d\, p}{d\, y} \frac{d\, T}{d\, y} + \frac{2}{3} \frac{\omega_5\, \mu^2}{\rho(y)\, T(y)^2} \left(\frac{d\, T}{d\, y}\right)^2 + \frac{1}{12} \frac{\omega_6\, \mu^2}{p(y)} \\
&\quad \times \left(\frac{d\, u}{d\, y}\right)^2, \\
\mathbf{q}^{(2)}_x &= \frac{1}{2} \frac{\theta_3\, \mu^2}{\rho(y)\, p(y)} \frac{d\, p}{d\, y} \frac{d\, u}{d\, y} + \frac{1}{2} \frac{\theta_4\, \mu^2}{\rho(y)} \frac{d^2\, u}{d\, y^2} + \frac{3}{2} \frac{\theta_5\, \mu^2}{\rho(y)\, T(y)} \\
&\quad \times \frac{d\, T}{d\, y} \frac{d\, u}{d\, y}, \quad \mathbf{q}^{(2)}_y = 0, \quad \mathbf{q}^{(2)}_z = 0.
\end{aligned}
\qquad (13)
$$

Note that there is a heat flow along the x direction but it does not give a contribution to the conservation equations, the reason being that in the energy conservation equation one has to evaluate the divergence of the heat flow and only the y component of the heat flux can contribute.

The x component in the momentum conservation is the same as the Navier-Stokes result because $\mathbf{P}^{(2)}_{yx} = 0$. Similarly the z component of momentum conservation is not altered so only the y component of momentum conservation is altered in the Burnett regime. Since this component must be a constant we see from the previous equations that the result is a second order ordinary differential equation for p. In the previous equation for $\mathbf{P}_{yy}$ there appears the second derivative for the temperature, which can be obtained from eq. (10). Using this result, we are lead to solve the following reduced second order system of ordinary differential equations:

$$
\begin{aligned}
\frac{d^2 u^\star}{d\, s^2} &= -\frac{1}{2\, T^\star(s)} \frac{d\, T^\star}{d\, s} \frac{d\, u^\star}{d\, s} + \frac{b_0\, p^\star(s)}{T^{\star\, 3/2}(s)}, \\
\frac{d^2 T^\star}{d\, s^2} &= \frac{8\, c_\mu}{15\, c_\lambda} \left(\frac{d\, u^\star}{d\, s}\right)^2 - \frac{1}{2\, T^\star(s)} \left(\frac{d\, T^\star}{d\, s}\right)^2,
\end{aligned}
\qquad (14)
$$

$$
\begin{aligned}
\frac{d^2 p^\star}{d\, s^2} &= \frac{b_1\, p^{\star(s)\, 2}}{T^{\star\, 2}(s)} + \frac{b_2\, p^{\star\, 2}(s)}{T^{\star\, 2}(s)} - \frac{b_1\, p^{\star\, 3}(s)}{T^{\star\, 2}(s)} \\
&\quad + \frac{1}{p^\star(s)} \left(\frac{d\, p^\star}{d\, s}\right)^2 - \frac{1}{T^\star(s)} \frac{d\, p^\star}{d\, s} \frac{d\, T^\star}{d\, s} \\
&\quad - \frac{9\, p^\star(s)}{4\, T^\star(s)} \left(\frac{d\, u^\star}{d\, s}\right)^2 - \frac{8\, \omega_3\, p^\star(s)\, c_\mu}{15\, \omega_2\, T^\star(s)\, c_\lambda} \left(\frac{d\, T^\star}{d\, s}\right)^2 \\
&\quad - \frac{p^\star(s)\, \omega_3}{2\, \omega_2\, T^{\star\, 2}(s)} \left(\frac{d\, T^\star}{d\, s}\right)^2 + \frac{\omega_4}{\omega_2\, T^\star(s)} \frac{d\, p^\star}{d\, s} \frac{d\, T^\star}{d\, s} \\
&\quad + \frac{\omega_5\, p^\star(s)}{\omega_2\, T^{\star\, 2}(s)} \left(\frac{d\, T^\star}{d\, s}\right)^2 + \frac{\omega_6\, p^\star(s)}{\omega_2\, T^\star(s)} \left(\frac{d\, u^\star}{d\, s}\right)^2,
\end{aligned}
\qquad (15)
$$

where $s = y/L$, $p^\star(s) = p(y)/p(0)$, $T^\star(s) = T(y)/T_R$ with T_R the temperature of the walls and $u^\star(y) = u(y)/(2kT_R/m)^{1/2}$. The coefficients are

$$b_0 = -\frac{8}{5}\frac{L^2\, a\sqrt{2\pi}\, p(0)\, m\,\sigma^2}{c_\mu\, k^2\, T_R^2},\quad b_1 = -\frac{384}{25}\frac{L^2\, p(0)\,\pi\,\sigma^4}{\omega_2\, c_\mu^2\, T_R^2\, k^2},$$
$$b_2 = \frac{L^2\,\frac{d^2 p}{d\,y2}(0)\, T(0)^2}{p(0)\, T_R^2}. \tag{16}$$

for symmetric profiles. Though the physical system is geometrically symmetry about the x axis this does not guarantee a symmetric profile since spontaneous symmetry breaking may occur [2]. However, the profiles measured in our DSMC computer experiments are in good agreement with this assumed symmetry.

In terms of the variables; $\mathbf{Y}_1(s) = u^\star(s)$, $\mathbf{Y}_2(s) = T^\star(s)$, $\mathbf{Y}_3(s) = p^\star(s)$, $\mathbf{Y}_4(s) = \frac{d\,u}{d\,s}$, $\mathbf{Y}_5(s) = \frac{d\,T^\star}{d\,s}(s)$ and $\mathbf{Y}_6(s) = \frac{d\,p^\star}{d\,s}(s)$, the previous system of three second order differential equations can be expressed as a system of six coupled first order differential equations, $\dot{\mathbf{Y}} = \mathbf{F}(\mathbf{Y})$, where the dot denotes the derivative with respect to s. The vector field $\mathbf{F}$ is given by:

$$\begin{aligned}
&\mathbf{F}_1(\mathbf{Y}) = \mathbf{Y}_4,\quad \mathbf{F}_2(\mathbf{Y}) = \mathbf{Y}_5,\quad \mathbf{F}_3(\mathbf{Y}) = \mathbf{Y}_6,\\
&\mathbf{F}_4(\mathbf{Y}) = -\frac{1}{2}\frac{\mathbf{Y}_4\,\mathbf{Y}_5}{\mathbf{Y}_2} + b_0\,\frac{\mathbf{Y}_3}{\mathbf{Y}_2^{3/2}},\\
&\mathbf{F}_5(\mathbf{Y}) = \frac{8\,c_\mu}{15\,c_\lambda}\mathbf{Y}_4^2 - \frac{1}{2}\frac{\mathbf{Y}_5^2}{\mathbf{Y}_2},\\
&\mathbf{F}_6(\mathbf{Y}) = b_1\,\frac{\mathbf{Y}_3^2}{\mathbf{Y}_2^2} + b_2\,\frac{\mathbf{Y}_3^2}{\mathbf{Y}_2^2} - b_1\,\frac{\mathbf{Y}_3^3}{\mathbf{Y}_2^2} + \frac{\mathbf{Y}_6^2}{\mathbf{Y}_2} - \frac{\mathbf{Y}_6\mathbf{Y}_5}{\mathbf{Y}_2}\\
&\qquad - \frac{9}{4}\frac{\mathbf{Y}_3\mathbf{Y}_4^2}{\mathbf{Y}_2} - \frac{8\,c_\mu\,\omega_3}{15\,c_\lambda\,\omega_2}\frac{\mathbf{Y}_3\mathbf{Y}_4^2}{\mathbf{Y}_2} - \frac{\omega_3}{2\,\omega_2}\frac{\mathbf{Y}_3\mathbf{Y}_5^2}{\mathbf{Y}_2}\\
&\qquad + \frac{\omega_4}{\omega_2}\frac{\mathbf{Y}_6\mathbf{Y}_5}{\mathbf{Y}_2} + \frac{\omega_5}{\omega_2}\frac{\mathbf{Y}_3\mathbf{Y}_5^2}{\mathbf{Y}_2^2} + \frac{\omega_6}{4\,\omega_2}\frac{\mathbf{Y}_3\mathbf{Y}_4^2}{\mathbf{Y}_2}.
\end{aligned} \tag{17}$$

where for simplicity the explicit s dependence is omitted.

To have a well posed problem requires the specification of initial or boundary conditions. For the Burnett equations, several issues regarding boundary conditions are still unresolved. Rather than looking at this point in a general setting it is important to know first if the Burnett equations can indeed reproduce the features observed in problems for which the Navier-Stokes equations are susceptible to improvement and this is what we would like to test here for plane Poiseuille flow.

To avoid the difficulty of specifying boundary conditions at $y = \pm L$ ($s = \pm 1$) we use the centerline ($s = 0$) profile values measured in the DSMC simulations as the initial values for the previous first order system, eq. (17). The explicit initial conditions used are:

$$u^\star(0) = u_0,\quad T^\star(0) = T_0,\quad p^\star(0) = 1, \tag{18}$$

with the derivatives at $s = 0$ equal to zero and the values u_0, $p(0)$ and T_0 taken from the DSMC data. The dynamical system, eq. (17), is given in terms of quotients of differentiable functions so that it is differentiable in $U \equiv \mathbb{R}\times\mathbb{R}^+\times\mathbb{R}^+\times\mathbb{R}^3$, $\mathbb{R}$ being the real numbers and $\mathbb{R}^+$ the positive real numbers. In particular, it is locally Lipshitz in that set [9] so that the usual local existence and uniqueness theorem holds for the initial values used as long as they are elements of U [9,10]. We would like to emphasize that the Burnett equations will be solved with initial conditions provided by the DSMC data, in this way the question of slip at the bounaries is bypassed but the calculated profiles at the boundaries allow us to compare the predicted slip with the DSMC data.

Finally, the values of the coefficients are:

$$\begin{aligned}
&\omega_1 = 1.014\times\frac{4}{3}\left(\frac{7}{2}-\frac{1}{2}\right),\quad \omega_2 = 2\times 1.014,\\
&\omega_3 = 3\times 0.806,\quad \omega_4 = 0.681,\quad \omega_5 = \frac{3}{2}\times 0.806,\\
&\omega_6 = 8\times 0.928,\quad \theta_3 = -3.09,\quad \theta_4 = 2.418,\\
&\theta_5 = 8.3855.
\end{aligned} \tag{19}$$

Notice that the θ's are not needed for solving the differential equations but are used to evaluate the heat flux, also θ_1 and θ_2 do not appear in the expressions for the fluxes given by eqs. (refrelpupoia). The Navier-Stokes equations result from taking $\mathbf{F}_3 = 0$ and $\mathbf{F}_6 = 0$ in eqs. (17).

V. THE BURNETT DESCRIPTION FOR THE FLUXES.

In the previous section we saw that, unlike the Navier-Stokes equations, the Burnett description predicts a heat flow along the x direction that has no effect on the temperature profile. Since the computer experiments can measure momentum and heat flux it is useful to evaluate explicitly the Burnett expressions for the various components of these fluxes.

First consider the expression of the x component of the heat flux; from eqs. (13) we have,

$$\mathbf{q}_x^{(2)} = \frac{1}{2}\frac{\theta_3\,\mu^2}{\rho(y)\,p(y)}\frac{d\,p}{d\,y}\frac{d\,u}{d\,y} + \frac{1}{2}\frac{\theta_4\,\mu^2}{\rho(y)}\frac{d^2\,u}{d\,y^2} + \frac{3}{2}\frac{\theta_5\,\mu^2}{\rho(y)\,T(y)} \times\frac{d\,T}{d\,y}\frac{d\,u}{d\,y}. \tag{20}$$

The second derivative of the velocity can be evaluated from the Navier-Stokes results and the mass density can be eliminated from the equation of state giving,

$$\begin{aligned}
\mathbf{q}_x^{(2)} =\ & \frac{25}{512}\frac{\theta_3\,c_\mu^2\,k^2\,T(y)^2}{\pi\,\sigma^4\,p(y)^2}\frac{d\,p}{d\,y}\frac{d\,u}{d\,y} - \frac{25}{1024}\frac{\theta_4\,c_\mu^2\,k^2\,T(y)^2}{\pi\,\sigma^4\,p(y)^2}\\
&\times\frac{d\,T}{d\,y}\frac{d\,u}{d\,y} - \frac{5}{32}\frac{\theta_4\,c_\mu\,a\left(m\,k\,T(y)\right)^{1/2}}{\sqrt{\pi}\,\sigma^4}\\
&+\frac{75}{512}\frac{\theta_5\,c_\mu^2\,k^2\,T(y)^2}{\pi\,\sigma^4\,p(y)}\frac{d\,T}{d\,y}\frac{d\,u}{d\,y}.
\end{aligned} \tag{21}$$

In terms of the notation used for the dynamical system the reduced form of the x component of the heat flow reads,

$$\mathbf{q}_x^{(2)\star} \equiv \frac{\mathbf{q}_x^{(2)}}{\frac{2\sqrt{2}(k\,T_R/m)^{3/2}}{\sigma^3}} = \frac{d_1\,Y_2^2\,Y_4\,Y_6}{Y_3^2} + \frac{d_2\,Y_2\,Y_4\,Y_5}{Y_3} + d_3\sqrt{Y}_2 + \frac{d_4\,Y_2\,Y_4\,Y_5}{Y_3^2}, \tag{22}$$

where,

$$d_1 = \frac{25}{1024}\frac{k\,T_R\,\theta_3\,c_\mu^2}{\sigma\,\pi\,p(0)\,L^2}, \quad d_2 = -\frac{25}{2048}\frac{k\,T_R\,\theta_4\,c_\mu^2}{\sigma\,\pi\,p(0)\,L^2},$$
$$d_3 = -\frac{5}{128}\frac{\sigma\,\sqrt{2}\,\theta_4\,c_\mu\,a\,m}{k\,T_R\,\sqrt{\pi}}, \quad d_4 = +\frac{75}{1024}\frac{k\,T_R\,\theta_5\,c_\mu^2}{\sigma\,\pi\,p(0)\,L^2}.$$

Since according to eq. (7) there is no x component of the heat flux at the Navier-Stokes regime we conclude that the x component of the total heat flux ($\mathbf{q}_x^T$), meaning the Navier-Stokes plus the Burnett contributions, is given by $\mathbf{q}_x^T = \mathbf{q}_x^{NS} + \mathbf{q}_x^{(2)} = \mathbf{q}_x^{(2)}$. Similarly we obtain that,

$$\mathbf{q}_y^{T\,\star} \equiv \frac{\mathbf{q}_y^T}{\frac{2\sqrt{2}(k\,T_R/m)^{3/2}}{\sigma^3}} = d_5\,\sqrt{Y}_2\,Y_5,$$
$$\mathbf{q}_z^{T\,\star} = 0, \tag{23}$$

where,

$$d_5 = -\frac{75}{256}\,\frac{c_\lambda\,\sigma\,\sqrt{2}}{L\,\sqrt{\pi}}. \tag{24}$$

Several components of the pressure tensor can be treated in a similar way to obtain,

$$\mathbf{P}_{zx}^{T\star} \equiv \frac{\mathbf{P}_{zx}^{NS} + \mathbf{P}_{zx}^{(2)}}{p(0)} = 0, \quad \mathbf{P}_{zy}^{T\star} \equiv \frac{\mathbf{P}_{zy}^{NS} + \mathbf{P}_{zy}^{(2)}}{p(0)} = 0,$$
$$\mathbf{P}_{yx}^{T\star} \equiv \frac{\mathbf{P}_{yx}^{NS} + \mathbf{P}_{yx}^{(2)}}{p(0)} = d_6\,\sqrt{Y}_2\,Y_4,$$
$$\mathbf{P}_{yy}^{T\star} \equiv \frac{\mathbf{P}_{yy}^{NS} + \mathbf{P}_{yy}^{(2)}}{p(0)} = d_7,$$
$$\mathbf{P}_{xx}^{T\star} \equiv \frac{\mathbf{P}_{xx}^{NS} + \mathbf{P}_{xx}^{(2)}}{p(0)} = \frac{3}{2}Y_3 - \frac{1}{2} + d_8 + \frac{d_9\,Y_2}{Y_3}\,Y_4^2,$$
$$\mathbf{P}_{zz}^{T\star} \equiv \frac{\mathbf{P}_{zz}^{NS} + \mathbf{P}_{zz}^{(2)}}{p(0)} = 3\,Y_3 - d_7 - \mathbf{P}_{xx}^{T\star}, \tag{25}$$

where,

$$d_6 = -\frac{5}{16}\frac{\sqrt{2}\,c_\mu\,k\,T_R}{\sqrt{\pi}\,\sigma^2\,L\,p(0)}, \; d_7 = 1 - \frac{25}{384}\frac{\omega_2\,c_\mu^2\,b_2\,T_R^2\,k^2}{L^2\,p(0)^2\,\pi\sigma^4},$$
$$d_8 = \frac{25}{768}\frac{\omega_2\,c_\mu^2\,b_2\,T_R^2\,k^2}{L^2\,p(0)^2\,\pi\,\sigma^2},$$
$$d_9 = \frac{25}{1024}\frac{c_\mu^2\,k^2\,T_R^2(\omega_6 - \omega_2)}{\pi\sigma^4\,p(0)^2\,L^2}, \tag{26}$$

and b_2 is given by eq. (16).

VI. THE DIRECT SIMULATION MONTE CARLO METHOD.

Direct simulation Monte Carlo (DSMC) is a well-established algorithm for computing gas dynamics at the level of Kinetic theory. For completeness, this section presents a brief summary of the method; it is described in detail in [11], see [12] for a tutorial, and [13,14] for reviews. Wagner [15] has proven that DSMC is equivalent to a stochastic evaluation of the Boltzmann equation.

In DSMC, the state of the system is given by the positions and velocities of particles, $\{\mathbf{r}_i, \mathbf{v}_i\}$. First, the particles are moved as if they did not interact, that is, their positions are updated to $\mathbf{r}_i + \mathbf{v}_i\Delta t + \frac{1}{2}\mathbf{a}\Delta t^2$, where Δt is the time step. A particle that strikes the thermal walls at $y = \pm L$ has its velocity replaced with a random value generated from the biased Maxwell-Boltzmann distribution; the system is periodic in the x and z directions. Second, after all particles have moved, a given number are randomly selected for collisions. This splitting of the evolution between streaming and collisions is accurate if the time step, $\Delta t \ll \tau$, where τ is the mean collision time for a particle.

The concept of "collision" implies that the interaction potential between particles is short-ranged. In the simulations presented here the particles are taken to be rigid spheres of diameter σ so, $\tau = m/\rho\pi\sigma^2\langle v_r\rangle$ where $\langle v_r\rangle$ is the average relative speed among the particles. The number of collisions among N particles during a time step is $M = \frac{1}{2}N\Delta t/\tau$. We use Bird's "no time counter" method [11] for determining M since it avoids the explicit evaluation of $\langle v_r\rangle$.

Particles are randomly selected as collision partners with the restriction that their mean separation be a fraction of a mean free path, $\ell = \langle v\rangle\tau$ [16]. This restriction is typically enforced by sorting the particles into cells whose dimensions are smaller than a mean free path. For hard spheres, the probability of selecting a given pair is proportional to the relative speed between the particles. DSMC evaluates individual collisions stochastically, conserving momentum and energy and selecting the post-collision angles from their kinetic theory distributions. For hard spheres, the center of mass velocity and relative speed are conserved in the collision with the direction of the relative velocity uniformly distributed in the unit sphere. This Markov approximation of the collision process is statistically accurate so long as the number of particles in a collision cell is sufficiently large, typically over twenty [17,18].

We define the average density of $f(\mathbf{v})$ as

$$\langle f(\mathbf{v})\rangle_y = \frac{1}{N_t}\sum_t^{N_t}\frac{1}{V_c}\sum_{i\in c} f(\mathbf{v}_i(t)) \tag{27}$$

where $\mathbf{v}_i$ is the velocity of particle i and N_t is the number of time steps over which samples are taken. The inner sum is over all particles within cell c, which has volume V_c and is centered at position y. The hydrodynamic variables are defined as

$$\rho(y) = \langle m\rangle_y \tag{28}$$
$$\mathbf{u}(y) = \langle m\mathbf{v}\rangle_y/\rho \tag{29}$$
$$T(y) = \frac{2m}{3k\rho}\left(\frac{1}{2}\langle mv^2\rangle_y - \frac{1}{2}\rho u^2\right) \tag{30}$$

and $p = \rho kT/m$. The fluxes are defined as

$$\begin{aligned}\mathbf{P}_{\alpha\beta}(y) &= \langle m(\mathbf{v}_\alpha - \mathbf{u}_\alpha)(\mathbf{v}_\beta - \mathbf{u}_\beta)\rangle_y \qquad (31)\\ &= \langle m\mathbf{v}_\alpha\mathbf{v}_\beta\rangle_y - \rho\mathbf{u}_\alpha\mathbf{u}_\beta\\ \mathbf{q}_\alpha(y) &= \frac{1}{2}\langle m(\mathbf{v}_\alpha - \mathbf{u}_\alpha)|\mathbf{v}-\mathbf{u}|^2\rangle_y \qquad (32)\\ &= \frac{1}{2}\langle m\mathbf{v}_\alpha v^2\rangle_y - \langle m\mathbf{v}_\alpha\mathbf{v}_\gamma\rangle_y\mathbf{u}_\gamma\\ &\quad +\rho\mathbf{u}_\alpha u^2 - \frac{1}{2}\mathbf{u}_\alpha\langle mv^2\rangle_y\end{aligned}$$

where α, β and γ are x, y, or z with implied summation over γ.

VII. SIMULATION RESULTS

To simplify comparison with the DSMC data in [5], for all the simulations $m = \sigma = T_R = 1$ and $k = \frac{1}{2}$. The sound speed at equilibrium is $\sqrt{5kT_R/3m} = 1.29$. The equilibrium density is $\rho_0 = 1.21\times 10^{-3}$ giving a mean free path of $\ell_0 = 186$.

A. The ten mean free path case.

To simplify comparison with the DSMC data in [5], the pressure is normalized by $(7.13394\times 10^{-4})\times 2\,kT_R/\sigma^3$ to make $p^\star(0) = 1$. The simulations were done for an acceleration of $a = 1.6\times 10^{-4}\times 2\,kT_R/m\,\sigma$ and a system size of $L = 1860\sigma = 10\ell_0$. Using these values we obtain,

$$\begin{aligned}&b_0 = -6.235007643, \quad b_1 = -162.3309911,\\ &d_1 = -0.50220358\times 10^{-5},\\ &d_2 = -0.1964932454\times 10^{-5},\\ &d_3 = -0.2450273776\times 10^{-4},\\ &d_4 = +0.408857099\times 10^{-4},\\ &d_5 = -0.1288339708\times 10^{-3},\\ &d_6 = -0.09546098954,\\ &d_9 = 0.006146583954.\end{aligned} \tag{33}$$

The coefficient b_2 was determined in such a way that the solution to the differential equations reproduced the qualitative behavior for the DSMC pressure profiles. The explicit value used is:

$$b_2 = 0.845, \tag{34}$$

from which we obtain,

$$d_7 = 0.9947945861,\ d_8 = 0.002602706959. \tag{35}$$

Finally the initial conditions used are:

$$u^\star(0) = 0.90287, \quad T^\star(0) = 1.2052, \quad p^\star(0) = 1.0, \tag{36}$$

with the derivatives at the center of the channel equal to zero. The simulation contained 2.5×10^4 particles and evaluated 2.5×10^8 collisions with statistical samples taken during the latter 1.2×10^8 collisions. The results for the profiles of the normal variables and some moments are given in figures 1-14.

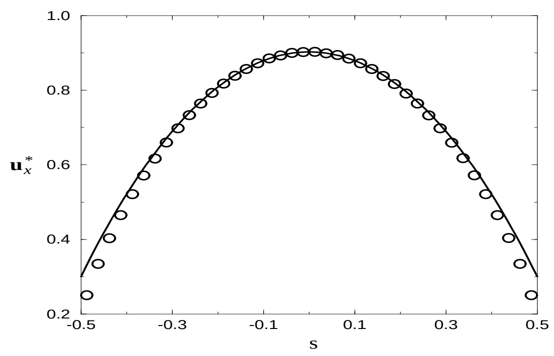

FIG. 1. Reduced velocity profile for the x component of the velocity vector $u^\star$ *vs.* s for $L = 10\ell_0$ system. Circles: DSMC, the error bars are smaller than the size of the symbols; Solid line: Burnett.

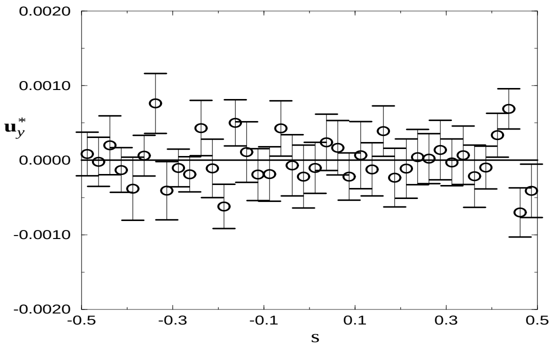

FIG. 2. Reduced velocity profile for the y component of the velocity vector $\mathbf{u}_y^\star$ *vs.* s for $L = 10\ell_0$ system. Circles: DSMC; Solid line: Assumption for plane Poiseuille flow.

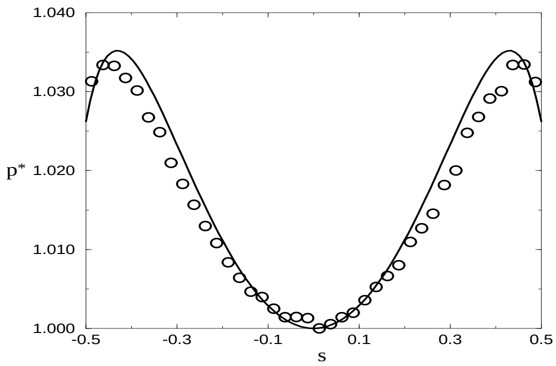

FIG. 5. Reduced pressure profile $p^\star$ *vs.* s for $L = 10\ell_0$ system. Circles: DSMC, the error bars are of approximately the same size as the symbols; Solid line: Burnett.

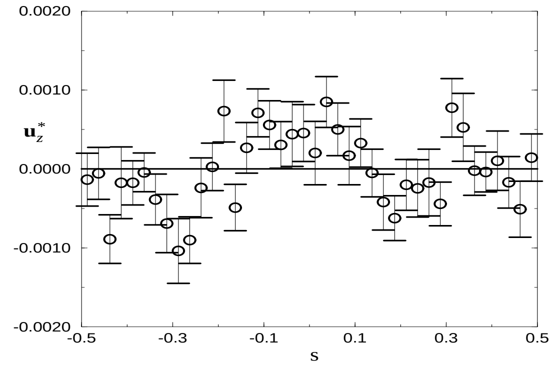

FIG. 3. Reduced velocity profile for the z component of the velocity vector $\mathbf{u}_z^\star$ *vs.* s for $L = 10\ell_0$ system. Circles: DSMC; Solid line: Assumption for plane Poiseuille flow.

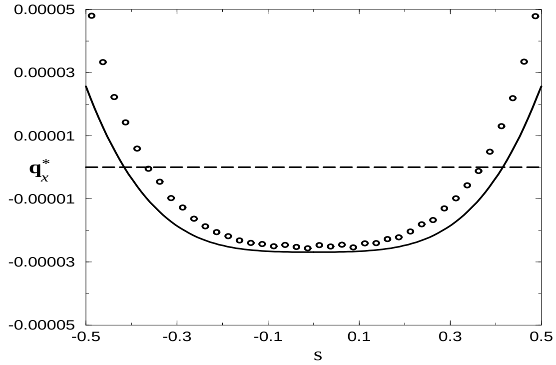

FIG. 6. Reduced x component of the heat flux, $\mathbf{q}_x^\star$ *vs.* s for $L = 10\ell_0$ system. Circles: DSMC; Solid line, the error bars are approximately three fourths of the size of the symbols: Burnett; Long dashed line: Navier-Stokes.

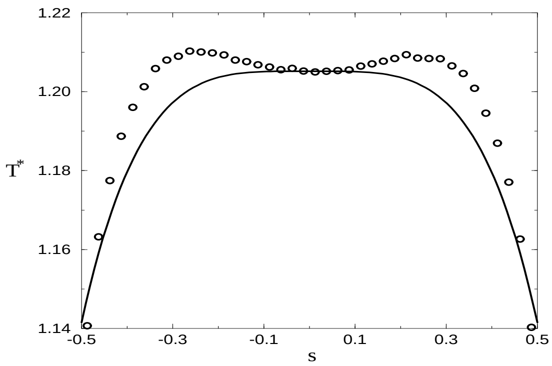

FIG. 4. Reduced temperature profile $T^\star$ *vs.* s for $L = 10\ell_0$ system. Circles: DSMC, the error bars are of approximately the same size as the symbols; Solid line: Burnett.

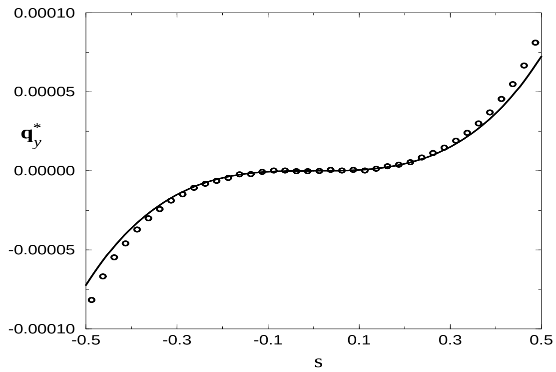

FIG. 7. Reduced y component of the heat flux, $\mathbf{q}_y^\star$ *vs.* s for $L = 10\ell_0$ system. Circles: DSMC, the error bars are approximately half of the size of the symbols; Solid line: Burnett.

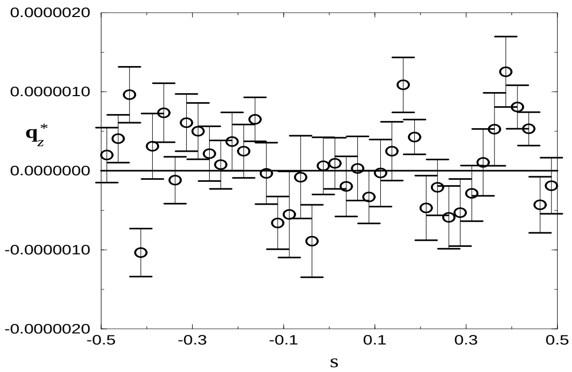

FIG. 8. Reduced z component of the heat flux, $\mathbf{q}_z^\star$ *vs.* s for $L = 10\ell_0$ system. Circles: DSMC; Solid line: Burnett and Navier-Stokes.

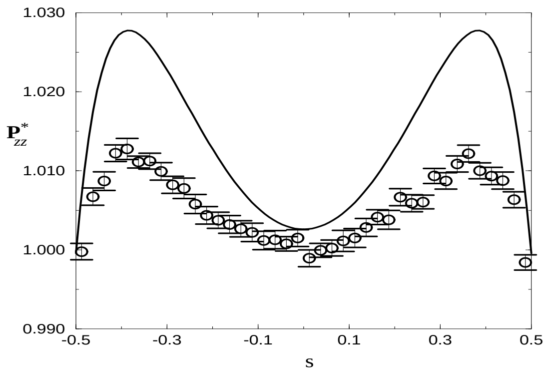

FIG. 11. Reduced zz component of the pressure tensor, $\mathbf{P}_{zz}^\star$ *vs.* s for $L = 10\ell_0$ system. Circles: DSMC; Solid line: Burnett.

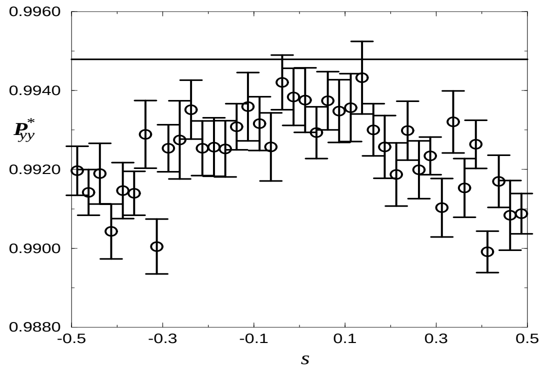

FIG. 9. Reduced yy component of the pressure tensor, $\mathbf{P}_{yy}^\star$ *vs.* s for $L = 10\ell_0$ system. Circles: DSMC; Solid line: Burnett.

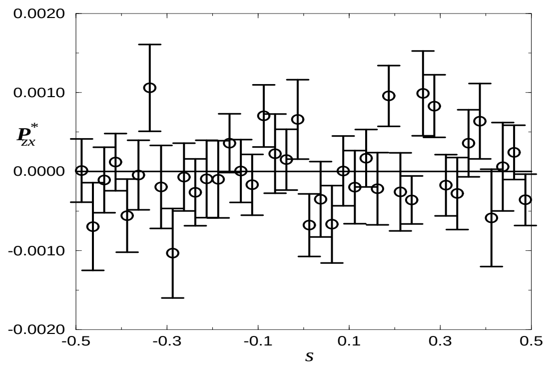

FIG. 12. Reduced zx component of the pressure tensor, $\mathbf{P}_{zx}^\star$ *vs.* s for $L = 10\ell_0$ system. Circles: DSMC; Solid line: Burnett.

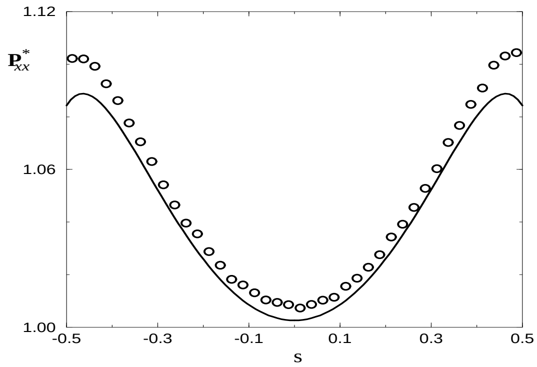

FIG. 10. Reduced xx component of the pressure tensor, $\mathbf{P}_{xx}^\star$ *vs.* s for $L = 10\ell_0$ system. Circles: DSMC, the error bars are of approximately the same size as the symbols; Solid line: Burnett.

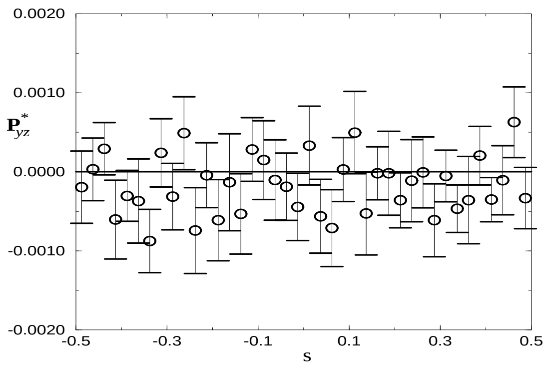

FIG. 13. Reduced yz component of the pressure tensor, $\mathbf{P}_{yz}^\star$ *vs.* s for $L = 10\ell_0$ system. Circles: DSMC; Solid line: Burnett and Navier-Stokes.

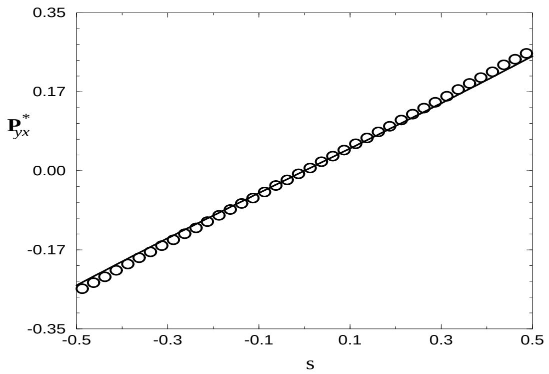

FIG. 14. Reduced yx component of the pressure tensor, $\mathbf{P}^\star_{yx}$ *vs.* s for $L = 10\ell_0$ system. Circles: DSMC, the error bars are a small fraction of the size of the symbols; Solid line: Burnett.

B. The twenty mean free path case.

For comparison with the DSMC data in [5], the pressure is normalized by $(6.727 \times 10^{-4}) \times 2\,k\,T_R\,/\sigma^3$ to make $p^\star(0) = 1$. The simulations were done for an acceleration of $a = 4.0 \times 10^{-5} \times 2\,k\,T_R\,/m\,\sigma$ and a system size of $L = 3720 \times \sigma = 20\ell_0$. Using these values we obtain,

$$\begin{aligned} b_0 &= -5.879345273, \quad b_1 = -577.3582581,\\ d_1 &= -0.1331459123 \times 10^{-5},\\ d_2 &= -0.5209495406 \times 10^{-6},\\ d_3 &= -0.6125684441 \times 10^{-5},\\ d_4 &= +0.1083975775 \times 10^{-4},\\ d_5 &= -0.6441653536 \times 10^{-4},\\ d_6 &= -0.05061788107,\\ d_9 &= 0.001728183586. \end{aligned} \tag{37}$$

The coefficient b_2 was determined in such a way that the solution to the differential equations reproduced the qualitative behavior for the DSMC pressure profiles. The explicit value used is:

$$b_2 = 0.2344, \tag{38}$$

from which we obtain,

$$d_7 = 0.9995940129, \quad d_8 = 0.0002029935458. \tag{39}$$

Finally the initial conditions used are:

$$u^\star(0) = 0.7575, \quad T^\star(0) = 1.1293, \quad p^\star(0) = 1.0, \tag{40}$$

with the derivatives at the center of the channel equal to zero. The simulation contained 5.0×10^4 particles and evaluated 5.0×10^8 collisions with statistical samples taken during the latter 2.5×10^8 collisions. The results for the profiles of the normal variables and some moments are given in figures 15-25.

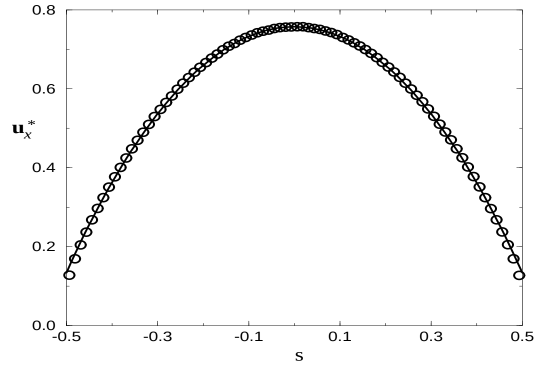

FIG. 15. Reduced velocity profile for the x component of the velocity vector $u^\star$ *vs.* s for $L = 20\ell_0$ system. Circles: DSMC, the error bars are a small fraction of the size of the symbols; Solid line: Burnett.

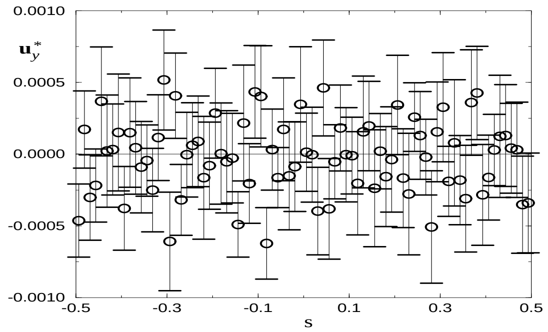

FIG. 16. Reduced velocity profile for the y component of the velocity vector $v^\star$ *vs.* s for $L = 20\ell_0$ system. Circles: DSMC; Solid line: Conservation.

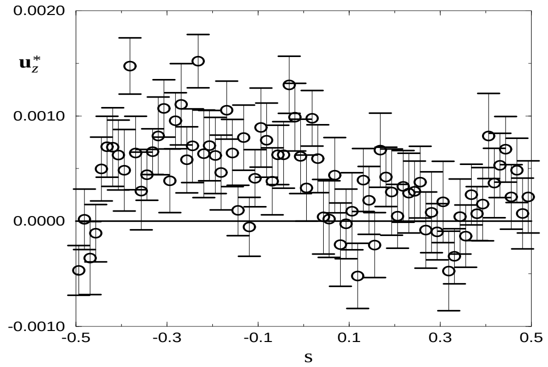

FIG. 17. Reduced velocity profile for the z component of the velocity vector $w^\star$ *vs.* s for $L = 20\ell_0$ system. Circles: DSMC; Solid line: Conservation.

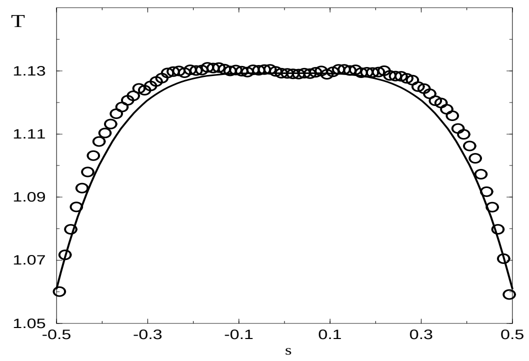

FIG. 18. Reduced temperature profile $T^\star$ *vs.* s for $L = 20\ell_0$ system. Circles: DSMC; Solid line, the error bars are about the third part of the symbols: Burnett.

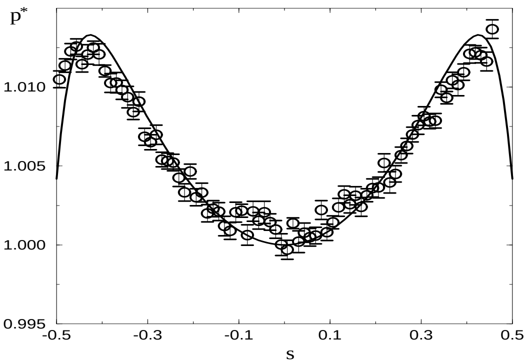

FIG. 19. Reduced pressure profile $p^\star$ *vs.* s for $L = 20\ell_0$ system. Circles: DSMC; Solid line: Burnett.

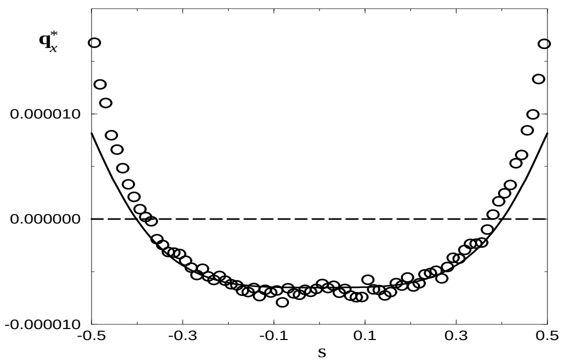

FIG. 20. Reduced x component of the heat flux, $\mathbf{q}_x^\star$ *vs.* s for $L = 20\ell_0$ system. Circles: DSMC, the error bars are of the same size as the symbols; Solid line: Burnett; Long dashed line: Navier-Stokes.

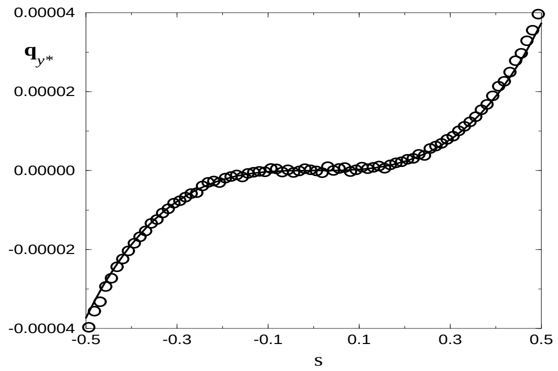

FIG. 21. Reduced y component of the heat flux *versus* s, $\mathbf{q}_y^\star$ *vs.* s for $L = 20\ell_0$ system. Circles: DSMC, the error bars are approximatly one fourth of the size of the symbols; Solid line: Burnett.

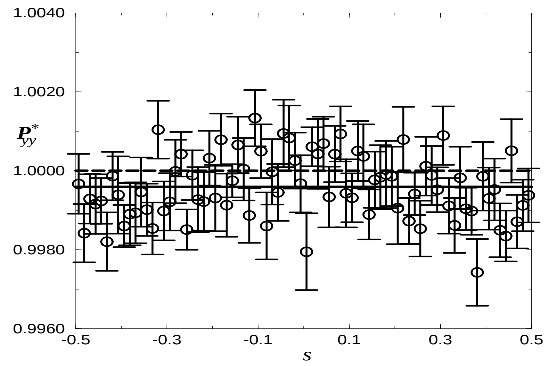

FIG. 22. Reduced yy component of the pressure tensor, $\mathbf{P}_{yy}^\star$ *vs.* s for $L = 20\ell_0$ system. Circles: DSMC; Solid line: Burnett.

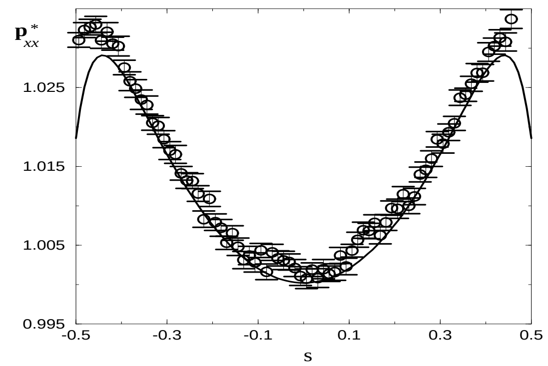

FIG. 23. Reduced xx component of the pressure tensor, $\mathbf{P}_{xx}^\star$ *vs.* s for $L = 20\ell_0$ system. Circles: DSMC; Solid line: Burnett; Long dashed line: Navier-Stokes.

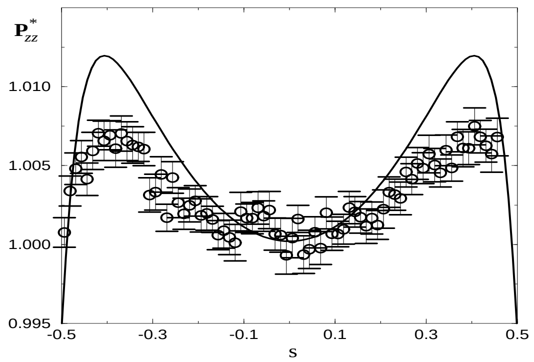

FIG. 24. Reduced zz component of the pressure tensor, $\mathbf{P}^\star_{zz}$ *vs.* s for $L = 20\ell_0$ system. Circles: DSMC; Solid line: Burnett; Long dashed line: Navier-Stokes.

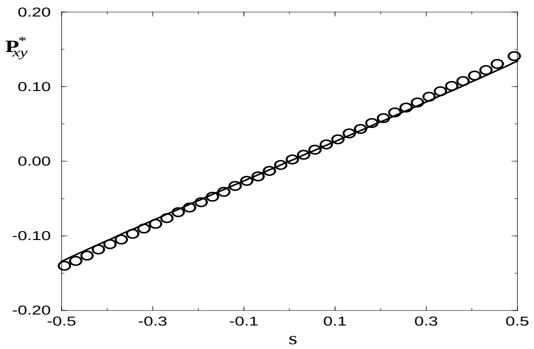

FIG. 25. Reduced yx component of the pressure tensor, $\mathbf{P}^\star_{yx}$ *vs.* s for $L = 20\ell_0$ system. Circles: DSMC, the error bars are approximately one fifth of the size of the symbols; Solid line: Burnett.

C. The forty mean free path case.

For comparison with the DSMC data in [5], the pressure is normalized by $(6.555 \times 10^{-4}) \times 2\,k\,T_R\,\sigma^3$ to make $p^\star(0) = 1$. The simulations were done for an acceleration of $a = 1.0 \times 10^{-5} \times 2\,k\,T_R\,/m\,\sigma$ and a system size of $L = 7440 \times \sigma = 40\ell_0$. Using these values we obtain,

$$\begin{aligned} b_0 &= -5.729018622, \quad b_1 = -2192.8448741, \\ d_1 &= -0.3415989901 \times 10^{-6}, \\ d_2 &= -0.1336547505 \times 10^{-6}, \\ d_3 &= -0.153142111 \times 10^{-5}, \\ d_4 &= +0.2781046924 \times 10^{-5}, \\ d_5 &= -0.00003220826771, \\ d_6 &= -0.02597303478, \\ d_9 &= 0.000455016712. \end{aligned} \tag{41}$$

The coefficient b_2 was determined in such a way that the solution to the differential equations reproduced the qualitative behavior for the DSMC pressure profiles. The explicit value used is:

$$b_2 = +0.05881696, \tag{42}$$

from which we obtain,

$$d_7 = 0.9999731778, \quad d_8 = 0.00001341110826. \tag{43}$$

Finally the initial conditions used are:

$$u^\star(0) = 0.689452, \quad T^\star(0) = 1.09814, \quad p^\star(0) = 1.0, \tag{44}$$

with the derivatives at the center of the channel equal to zero. The simulation contained 6.0×10^4 particles and evaluated 9.0×10^8 collisions with statistical samples taken during the latter 3.0×10^8 collisions. The results for the profiles of the normal variables and some moments are given in figures 26-36.

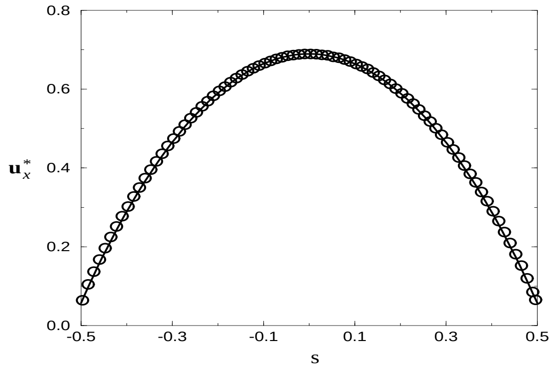

FIG. 26. Reduced velocity profile for the x component of the velocity vector $u^\star$ *vs.* s for $L = 40\ell_0$ system. Circles: DSMC, the error bars are a small fraction of the size of the symbols; Solid line: Burnett.

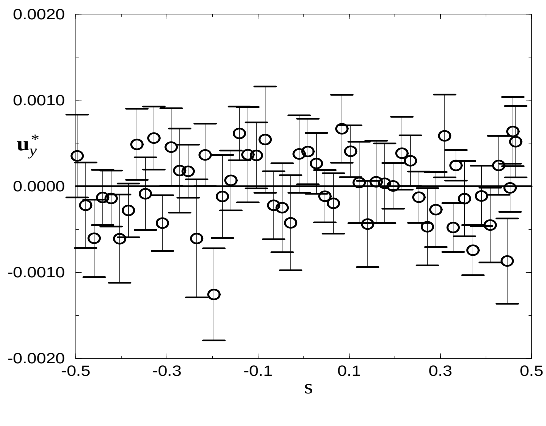

FIG. 27. Reduced velocity profile for the y component of the velocity vector $v^\star$ *vs.* s for $L = 40\ell_0$ system. Circles: DSMC; Conservation: Solid line.

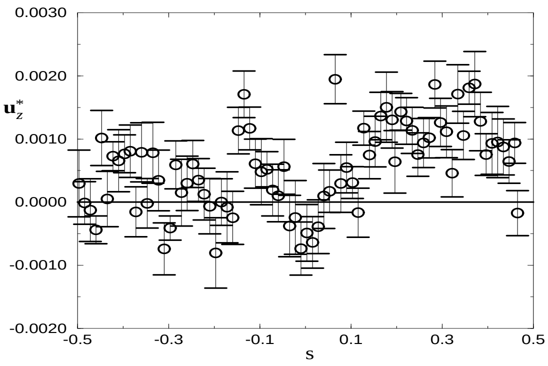

FIG. 28. Reduced velocity profile for the z component of the velocity vector $w^\star$ *vs.* s for $L = 40\ell_0$ system. Circles: DSMC; Conservation: Solid line.

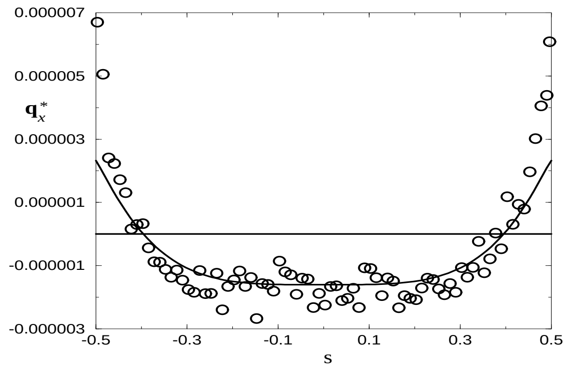

FIG. 31. Reduced x component of the heat flux, $\mathbf{q}_x^\star$ *vs.* s for $L = 40\ell_0$ system. Circles: DSMC, the error bars are about the size of the symbols; Solid line: Burnett; Long dashed line: Navier-Stokes.

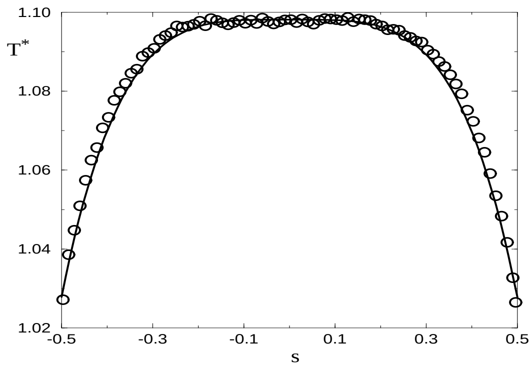

FIG. 29. Reduced temperature profile $T^\star$ *vs.* s for $L = 40\ell_0$ system. Circles: DSMC, the error bars are about a third of the size of the symbols; Solid line: Burnett.

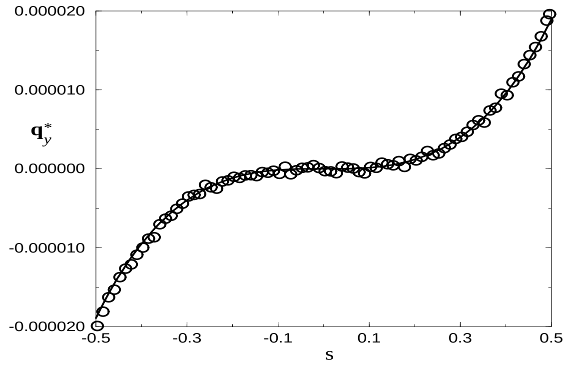

FIG. 32. Reduced y component of the heat flux, $\mathbf{q}_y^\star$ *vs.* s for $L = 40\ell_0$ system. Circles: DSMC, the error bars are about one fourth of the size of the symbols; Solid line: Burnett.

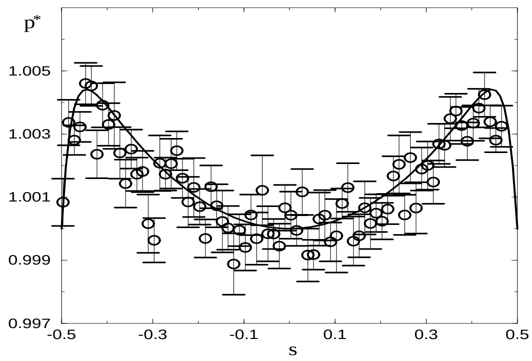

FIG. 30. Reduced pressure profile $p^\star$ *vs.* s for $L = 40\ell_0$ system. Circles: DSMC; Solid line: Burnett.

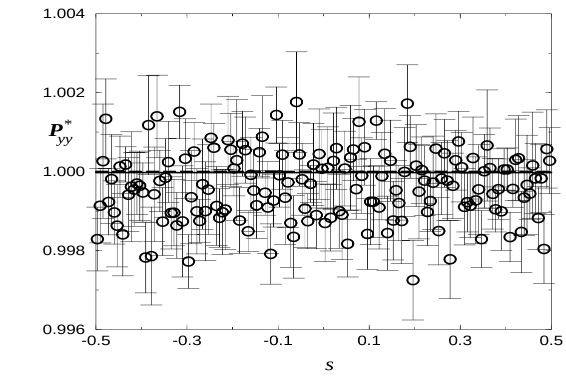

FIG. 33. Reduced yy component of the pressure tensor, $\mathbf{P}_{yy}^\star$ *vs.* s for $L = 40\ell_0$ system. Circles: DSMC; Solid line: Burnett.

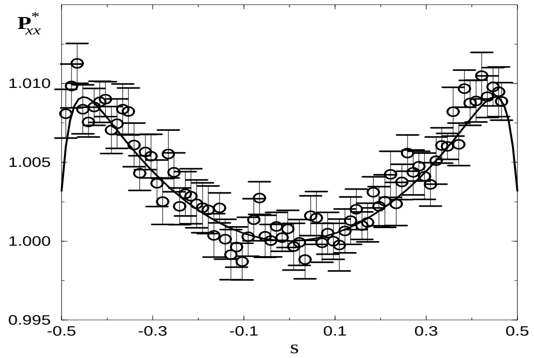

FIG. 34. Reduced xx component of the pressure tensor, $\mathbf{P}^{\star}_{xx}$ *vs.* s for $L = 40\ell_0$ system. Circles: DSMC; Solid line: Burnett.

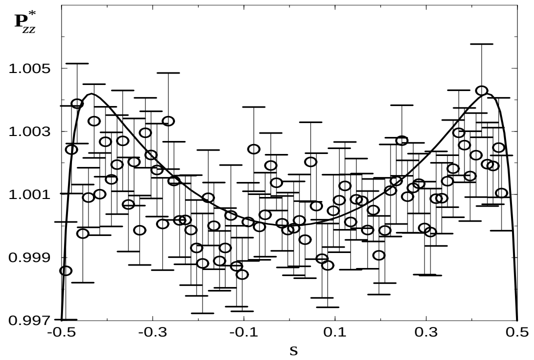

FIG. 35. Reduced zz component of the pressure tensor, $\mathbf{P}^{\star}_{zz}$ *vs.* s for $L = 40\ell_0$ system. Circles: DSMC; Solid line: Burnett.

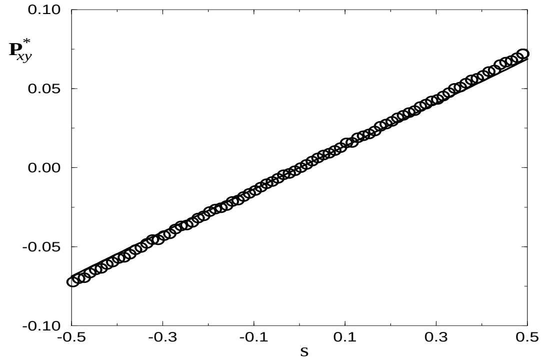

FIG. 36. Reduced yx component of the pressure tensor, $\mathbf{P}^{\star}_{yx}$ *vs.* s for $L = 40\ell_0$ system. Circles: DSMC, the error bars are about one fifth the size of the symbols; Solid line: Burnett.

VIII. ANALYSIS OF THE RESULTS

This section discusses the general features observed in the above DSMC data and the comparison with the continuum equations. In some cases the effects are subtle, which is the reason we provide numerous graphs where the reader can get a more detailed picture. In several cases (e.g., $\mathbf{u}_x$, T, $\mathbf{P}_{yx}$, $\mathbf{q}_y$) the profiles obtained from the Navier-Stokes equations and the Burnett equations are practically indistinguishable so only the latter **are** shown.

From figures 1, 15 and 26, we conclude that the profile for the x component of velocity is in reasonable agreement with the Burnett equations. The largest difference is observed at the highest Knudsen number, $K = \ell_0/L = 1/10$, where the discrepancy in the slip at the boundary is the most significant, in agreement with previous DSMC and MD results [19]. The $\mathbf{u}_x$ profiles predicted by the Burnett and Navier-Stokes equations are nearly identical so the latter **are** omitted in figs. 1, 15 and 26.

For plane Poiseuille flow we assumed that the other components of the hydrodynamic velocity to be zero and the measured profiles for $\mathbf{u}_y$ and $\mathbf{u}_z$ are shown in figures 2, 16, 27, 3, 17, and 28. For the velocity component perpendicular to the walls the DSMC data is consistent with the assumption that $\mathbf{u}_y = 0$. For the parallel component, $\mathbf{u}_z$, there is noticeable variation, especially in the $L = 40\ell_0$ system (fig. 28), because the long wavelength fluctuations in the periodic directions are very long lived. A similar effect is expected in $\mathbf{u}_x$ but is masked by the mean flow, which is nearly four orders of magnitude larger. Though it is possible that the stationary situation has not been established, this explanation seems unlikely since the DSMC data is assembled from a sequence of simulation runs, discarding any runs exhibiting remnants of the initial transient.

The most striking feature in the DSMC temperature profiles (figs. 4, 18 and 29) is the appearance of two local maxima, which is quite noticeable for the 10 mean free path case. The Burnett and Navier-Stokes equations give nearly identical predictions (the latter is omitted from figs. 4, 18 and 29) and fail to capture this bimodal behavior. However, the maximum difference between the DSMC data and the Burnett prediction is about 1% for the 10 mean free path case and the agreement improves with decreasing Knudsen number. This bimodal behavior is predicted in analyses using the BGK model [4] and Grad's expansion [26].

The pressure profiles, figs. 5, 19 and 30, all show good agreement between the DSMC data and the Burnett equations. This agreement, however, is constructed because in lieu of determining the **initial** conditions the coefficient b_2 is selected so as to fit the data. This coefficient depends on the second derivative of p at $s = 0$ but the DSMC data is not sufficiently accurate to extract its value. It turns out that the pressure profile obtained with the Burnett equations is sensitive to the value of b_2 but the velocity and temperature profiles are not affected. The Navier-Stokes equations predict that $p^\star(s) = 1$.

Next we examine the components of the heat flux and the complete pressure tensor. One goal is to infer, if possible, the origin of the bimodal temperature profile. From the general assumptions for plane Poiseuille flow ($\mathbf{u}_y = \mathbf{u}_z = 0$ and Landau's symmetry argument) the velocity, temperature and pressure profiles can depend only on $\mathbf{q}_y$, $\mathbf{P}_{yx}$ and $\mathbf{P}_{yy}$. However, to have a better understanding of the problem it is useful to examine all the components of $\mathbf{q}$ and $\mathbf{P}$ to obtain the leading moments of the distribution function. Furthermore, the three assumptions given in section II need to be tested.

The x component of the heat flux is zero according to the Navier-Stokes equations but is different from zero according to Burnett. Figures 6, 20 and 31 compare the Burnett prediction with the results from DSMC. The qualitative behavior of $\mathbf{q}_x$ is very similar, in particular the change in sign of the heat flux, and the agreement between Burnett and DSMC is better at lower Knudsen number. The discrepancy is greatest at the boundaries where larger gradients are present. Notice that even at the lowest Knudsen number the DSMC data clearly indicates that $\mathbf{q}_x \neq 0$. A non-zero parallel heat flux is also predicted in the BGK model [4] and Grad's expansion [26].

Figures 7, 21 and 32 show that y component of the heat flux, as predicted by Burnett and Navier-Stokes, is in good agreement with the DSMC data, the differences being greatest at large Knudsen numbers and near the boundaries where larger gradients are present. However, near the center of the system, where the bimodal behavior of the temperature is observed, the heat flow given by DSMC and Burnett are in good agreement, which indicates that the discrepancy in the temperature profiles probably cannot be explained in terms of the differences for $\mathbf{q}_y$. The DSMC results confirm that the z component of the heat flux is zero; results from the 10 mean free path system are shown in figure 8 and the data from the other cases is similar.

From Landau's symmetry argument and given that $\mathbf{u}_y = \mathbf{u}_z = 0$ it follows from the conservation equations that $\mathbf{P}_{yy}$ must be a constant. Fig. 9 shows that the DSMC data for the $L = 10\ell_0$ system exhibits a weak non-constant behavior and is about 0.2 % below the Burnett prediction. This could be an explanation for the discrepancy for the temperature profile, though for $L = 20\ell_0$ the DSMC temperature profile exhibits a bimodal behavior while $\mathbf{P}_{yy}$ is, within statistical error, a constant function (see figs. 22 and 33). A possible explanation for $\mathbf{P}_{yy}$ not being exactly constant in the $L = 10\ell_0$ system is that while, on average, $\mathbf{u}_y = \mathbf{u}_z = 0$, these components of velocity fluctuate and these non-equilibrium fluctuations have long-range spatial correlations [20]. The other diagonal components of the pressure tensor are not zero; the DSMC data and Burnett predictions for $\mathbf{P}_{xx}$ (figs. 10, 23 and 34) and $\mathbf{P}_{zz}$ (figs. 11, 24 and 35) are in qualitative agreement.

Finally we turn our attention to the off-diagonal elements of $\mathbf{P}$. The DSMC data confirms the Burnett and Navier-Stokes predictions that the components $\mathbf{P}_{xz}$ and $\mathbf{P}_{yz}$ are zero, as seen in figures 12 and 13 for the $L = 10\ell_0$ system with similar results for the other cases. From figures 14, 25 and 36, we see that $\mathbf{P}_{yx}$ is basically a linear function of s for both the DSMC data and the Burnett equations. The slopes differ slightly and while we do not expect that this explains the bimodal temperature profile **and** a more detailed analysis is needed.

IX. FINAL REMARKS.

From our results we conclude that the bimodal temperature profile observed in DSMC cannot be explained with the Burnett equations but that the non-constant pressure profile is a second order Knudsen effect. This conclusion is consistent with the fact that as the Knudsen number is lowered the bimodality in the temperature profile becomes unobservable while a significant non-constant pressure is still measured in DSMC [5]. The bimodal character of the temperature profiles is perhaps a super-Burnett effect, however it should be pointed out that the higher order Chapman-Cowling [7] gradient expansions are very complicated. While some work has been done with the super-Burnett equations [21] this work is restricted to linearized corrections to the fluxes. For these reasons it seems more promising to look for alternatives such as the regularization given by Rosenau [22] or the partial summation to the Chapman-Enskog method given by Gorban and Karlin [23]. These methods however have some restrictions, such as the use of a linearized collision operator.

Tij. *et al.* [24] investigated the present problem using moment methods for Maxwellian molecules and obtained the bimodal behavior for the temperature profiles. Unfortunately simulations of Poiseuille flow using Maxwellian molecules are still lacking so it is not known whether their prediction is quantitative. For the model used by Tij *et al.*, Ikenberry and Truesdell [25] have evaluated a broad set of kinetic quantities that allow one to compute many moments, but a similar analysis has not been performed for other potentials, such as rigid spheres. Tij *et al.* predicted a heat flux in the x direction, in qualitative agreement with the DSMC data and the Burnett results presented here. As we pointed out, this heat flux has no effect on the conservation equations, which are used to obtain the profiles. Recently Risso and Cordero [26] have used MD simulations and Grad's expansion method to reach some of the same conclusions as in this work.

While moment methods recover many of the qualitative features observed in Poiseiulle flow, their robustness has been criticized not only for the closure problem but also in evaluating shock waves. As Weiss [27] states (we have changed consistently the numbering of the references), "*The shock structure in monatomic gases is not satisfactorily described by the Navier-Stokes-Fourier theory, e.g., see [28]. But Grad's 13-moment theory is even worse; indeed, Grad [29,30] himself found that no continuous shock structure exists beyond Mach 1.65, which is the maximum speed of propagation of the 13-moment theory.*" Holway [31] has shown that no matter how many moments are taken into account there is no continuous continuous shock structure beyond Mach 1.85, though this result has been challenged by Weiss himself [32]. In contrast, Gilbarg and Paolucci [28] remark that, "*While the evidence from kinetic theory and the theory of nonlinear viscosity indicate that the Navier-Stokes equations yield values of the shock thickness that are perhaps smaller than the actual one, there is nothing in the evidence to suggest that the classical theory is far wrong.*" Finally, we would like to point out that for shock waves there is indeed substantial evidence that the Navier-Stokes theory is susceptible to improvement [6,11,33,34]. Rather than continuing to listing all points of view on this topic let us conclude by stating that a vigorous debate exists and that further experiments and simulations are needed to resolve these arguments.

DSMC simulations can provide detailed measurements of moments of the velocity distribution function but in the past such measurements were restricted to extremely non-equilibrium flows, such as strong shocks [11], for shock waves experimental information about the distribution function is also available [35]. This paper demonstrates that the heat flux and pressure tensor can differ measurably from their Navier-Stokes predictions and that the Burnett equations can do significantly better even in a simple, subsonic flow.

We would like to express our gratitude to R.M. Velasco for discussions held along the lines of this work. This work was supported in part by CONACyT (0651-E9110) and by a grant from the Fluid and Particle Processes program at the National Science Foundation.

---

[1] J.C. Maxwell, Philos. Trans. London **70**(1867)231.
[2] L. Rosenhead, Proc. Roy. Soc. London **A 175**(1940)436.
[3] P.G. Drazin and W.H. Reid, Hydrodynamic Stability (Cambridge University Press, 1985).
[4] M. Tij and A. Santos, J. Stat. Phys. **76**(1994)1399.
[5] M.M. Malek, F. Baras and A.L. Garcia, Physica **A240**(1997)255.
[6] F.J. Uribe, R.M. Velasco and L.S. García-Colín, Phys. Rev. Lett. (1998)
[7] S. Chapman & T.G. Cowling, The Mathematical Theory of Non-Uniform Gases (Cambridge University Press, 1970).
[8] L.D. Landau and E.M. Lifshitz, Fluid Mechanics (Pergamon Press, 1986).
[9] L. Loomis and S. Stenberg, Advanced Calculus,
[10] Y. Choquet-Bruhat, C. DeWitt-Morete and M. Dillard-Bleick, Analysis, Manifolds and Physics (North-Holland, Amsterdam, 1987).
[11] G.A. Bird, *Molecular Gas Dynamics and the Direct Simulation of Gas Flows* (Clarendon, Oxford, 1994).
[12] F. Alexander and A. Garcia, The Direct Simulation Monte Carlo Method, *Computers in Physics* **11**, 588 (1997).
[13] E.P. Muntz, Rarefied Gas Dynamics, *Ann. Rev. Fluid Mech.* **21**, 387 (1989).
[14] E.S. Oran, C.K. Oh, and B.Z. Cybyk, Direct Simulation Monte Carlo: Recent Advances and Applications, *Annu. Rev. Fluid Mech.* **30**, 403 (1998).
[15] W. Wagner, *J. Stat. Phys.* **66** 1011 (1992).
[16] F.J. Alexander, A.L. Garcia and B.J. Alder, Cell Size Dependence of Transport Coefficients in Stochastic Particle Algorithms, *Phys. Fluids* **10**, 1540 (1998).
[17] M. Fallavollita, D. Baganoff and J. McDonald, Reduction of Simulation Cost and Error for Particle Simulations of Rarefied Flows, *J. Comp. Phys.* **109**, 30 (1993)
[18] G. Chen and I. Boyd, Statistical Error Analysis for the Direct Simulation Monte Carlo Technique, *J. Comp. Phys.* **126**, 434 (1996).
[19] D. Morris, L. Hannon and A.L. Garcia, *Phys. Rev. A15* **46** 5279 (1992).
[20] A. Garcia, M. Malek Mansour, G. Lie and E. Clementi, *Phys. Rev. A* **36** 4348 (1987).
[21] C.S. Wang-Chang and G.E. Uhlenbeck, in Studies in Statistical Mechanics, ed. J. de Boer and G.E. Ulenbech, (North-Holland, Amsterdam,1970). p.1. ; C.S. Wang-Chang, *ibid*, p. 27.
[22] Rosenau, P., Phys. Rev. A **40**(1989)7193.
[23] Gorban, A.N. and Karlin, I.V., Phys. Rev. Lett. **77** (1996) 282.
[24] M. Tij, M. Sabbane and A. Santos, Phys. Fluids
[25] C. Truesdell and G. Muncaster, Fundamentals of Maxwell's Kinetic Theory of a simple Monatomic Gas (Academic Press, New York, 1980).
[26] D. Risso and P. Cordero, Phys. Rev. E 58 546-553 (1998).
[27] W. Weiss, Phys. Rev. **E 52**(1996)R5760.
[28] D. Gilbarg and D. Paolucci, J. Rat. Mech. Anal. **2**(1953)617.
[29] H. Grad, Commun. Pure Appl. Math. **5**(1952)257.
[30] H. Grad., in Thermodynamics of Gases, Handbuch der Physik Vol. 12, ed. S Flugge (Springer-Verlag, Berlin, 1958).
[31] L. H. Holway, Phys. Fluids **7**(1964)911.
[32] W. Weiss, Phys. Fluids **8**(1996)1689.
[33] H. Alsmeyer, J. Fluid Mech. **74**(1976)497.
[34] G. C. Pham-Van-Diep, D.A. Erwin and E.P. Muntz, J. Fluid Mech. **232**(1991)403.
[35] G. C. Pham-Van-Diep, D.A. Erwin and E.P. Muntz, Science **245**(1989)624.